The Astrophysical Journal Letters, 892:L27 (8pp), 2020 April 1 https://doi.org/10.3847/2041-8213/ab8012

Could Quasar Lensing Time Delays Hint to a Core Component in Halos, Instead of H_0 Tension?

Kfir Blum[1,2], Emanuele Castorina[2], and Marko Simonović[2]
[1] Weizmann Institute, Department of Particle Physics and Astrophysics, Rehovot 7610001, Israel; kfir.blum@weizmann.ac.il
[2] Theory Department, CERN, 1 Esplanade des Particules, Geneva 23, CH-1211, Switzerland; emanuele.castorina@cern.ch, marko.simonovic@cern.ch
Received 2020 February 24; revised 2020 March 13; accepted 2020 March 16; published 2020 April 2

Abstract

The time delay measured between the images of gravitationally lensed quasars probes a combination of the angular diameter distance to the source-lens system and the mass density profile of the lens. Observational campaigns to measure such systems have reported a determination of the Hubble parameter H_0 that shows significant tension with independent determination based on the cosmic microwave background (CMB) and large-scale structure (LSS). We show that lens mass models that exhibit a cored component, coexisting with a cusp, probe a degenerate direction in the lens model parameter space, being an approximate mass sheet transformation. This family of lens models has not been considered by the cosmographic analyses. Once added to the model, the cosmographic error budget should become dependent on stellar kinematics uncertainties. We propose that a core component coexisting with a cusp could bring the lensing measurements of H_0 into accordance with the CMB/LSS value.

Unified Astronomy Thesaurus concepts: Gravitational lensing (670); Strong gravitational lensing (1643); Hubble constant (758); Galaxy structure (622)

1. Introduction and Main Result

There appears to be a tension between measurements of the Hubble parameter H_0 based on the classic cosmic distance ladder method and measurements obtained through a fit of the standard ΛCDM model to the cosmic microwave background (CMB) or large-scale structure (LSS) data (for a summary, see Verde et al. 2019). The SH0ES collaboration (Riess et al. 2019) reported $H_0 = 74.03 \pm 1.42$ km s^{-1} Mpc^{-1} using supernovae calibrated with Cepheids. This result is more than 4σ discrepant with the best-fit ΛCDM value given by the Planck collaboration, $H_0 = 67.36 \pm 0.54$ km s^{-1} Mpc^{-1} (Planck Collaboration et al. 2018), or with H_0 measurements obtained from galaxy clustering and galaxy lensing data (Abbott et al. 2018; D'Amico et al. 2019; Ivanov et al. 2019; Tröster et al. 2019) that are independent of but agree with the CMB result. The tension is not so strong in the analysis of a supernova sample calibrated with the tip of the red giant branch, which gives $H_0 = 69.8 \pm 0.8(\text{stat}) \pm 1.7(\text{sys})$ km s^{-1} Mpc^{-1} (Freedman et al. 2019). On the other hand, a third, alternative method to constrain H_0 independently of both the distance ladder and cosmological perturbation theory, is provided by measurements of time delays in strongly lensed systems (Refsdal 1964; Kochanek 2002, 2006). The H0LiCOW collaboration (Suyu et al. 2017) used the time delays between multiple images of strongly lensed galaxies hosting a quasar to obtain $H_0 = 73.3^{+1.7}_{-1.8}$ km s^{-1} Mpc^{-1} (Suyu et al. 2017; Birrer et al. 2019; Bonvin et al. 2019; Chen et al. 2019; Wong et al. 2019), achieving 2.5% precision with a central value in agreement with SH0ES. Combining the SH0ES and H0LiCOW measurements, the result is in more than 5σ tension with CMB/LSS data.

Given the importance of these results to cosmology, it is worth investigating them from every angle. In this Letter we focus on the lensing time delay ("cosmography") measurements. It is well known that lensing analyses are subject to systematic uncertainty associated with the choice of the family of models used to reconstruct the lens potential (Falco et al. 1985; Schneider & Sluse 2013, 2014; Xu et al. 2016; Unruh et al. 2017; Tagore et al. 2018; Sonnenfeld 2018; Gomer & Williams 2019; Kochanek 2019). The H0LiCOW collaboration is, of course, well aware of this problem, and had taken measures to mitigate it by considering different families of lens models. Nevertheless, H0LiCOW systems probe the baryonic-dominated inner part of the lens, where theoretical understanding of the mass profile is limited to challenging hydrodynamical simulations. Moreover, given that we do not know what makes up the dark matter, its distribution on galactic scales could exhibit unexpected features. With these issues in mind, the question we address in this Letter is: could a feature in the mass density profile of H0LiCOW lenses bring the cosmographic result for H_0 to agree with the CMB/LSS value? Another way to phrase this question could be to accept, tentatively and for the purpose of the exercise, the CMB/LSS value of H_0; and then ask, given this hypothesis, what would the cosmography data teach us about the inner structure of galaxies.

We believe that we have found an interesting answer to this question. To summarize, we find that if one took the simple power-law (PL) density models, shown by H0LiCOW to provide a good fit to the lensing data, and then added a core component *in addition to* the PL, then: (i) the lensing reconstruction problem should be equally well solved by the PL+core models as it is for the pure PL; and (ii) the addition of comparable cores to all H0LiCOW lenses would systematically shift the inferred cosmographic value of H_0 downward in all systems, in accordance with the fact that all of the systems analyzed by the standard H0LiCOW analysis pipeline consistently hint to high H_0.

The cores we need are a moderate deformation of the nominal profile: at the Einstein radius (translating to a few kiloparsecs for H0LiCOW systems, where the lenses are massive elliptical galaxies), the core component need only make up 10% or less of the total enclosed mass of the lens.

Outside of the Einstein radius the relative core contribution could become larger, potentially reaching as much as $\mathcal{O}(1)$ of the mass and opening a possible way to constrain our solution with detailed kinematic modeling. However, current lensing data do not constrain very well the outer extent of the core.

Single-source lensing data cannot distinguish a pure PL profile from PL+core, because moving along the PL+core family of models (as we shall define in Section 2) is an approximate mass sheet transformation (MST; Falco et al. 1985). Therefore, PL +core models probe a flat direction in the likelihood for H_0. Stellar kinematics could, in principle, break the mass sheet degeneracy (MSD; Romanowsky & Kochanek 1999; Treu & Koopmans 2002; Jee et al. 2015, 2016; Shajib et al. 2018). However, as mentioned above, to solve the H_0 tension we need an effect of no more than 10% in enclosed mass within $\theta_{\rm E}$. Constraining this with stellar kinematics would not be trivial and would suffer from systematic uncertainties related to, e.g., the velocity anisotropy modeling. Furthermore, kinematics modeling uncertainties would come to dominate the determination of H_0, which should be revised (Kochanek 2019). Perhaps another potential way to resolve the MSD would be to have multiple sources lensed by the same object, as is usually the case in lensing by galaxy clusters (Grillo et al. 2018, 2020).

It is worth pointing out that we are not aware of the presence of PL+core profiles in simulations. In this sense, introducing them is an ad hoc solution of the (cosmographic contribution to) the H_0 tension. But we are also not aware of observational data that excludes such profiles. If one accepts PL+core profiles, then the question arises what is the core component made of. Since the inner part of the lenses is baryon-dominated, we do not know at this point if the core is some baryonic structure, or dark matter. It is exciting to speculate that the H_0 tension could actually hint to new constraints on the nature of the dark matter, perhaps along the lines of models such as in Schive et al. (2014) or Spergel & Steinhardt (2000).

This Letter is organized as follows. In Section 2 we show that adding an inner core component, on top of a (rescaled) cusp component, is an approximate MST. We give some simple examples, estimate the MSD-breaking effects, and introduce λPL models as a family of models that is expected to probe a flat direction in cosmographic measurements of H_0. In Section 3 we consider as input the CMB/LSS measurement of H_0 and use it to estimate the required morphology of H0LiCOW lenses. In Section 4 we discuss our findings, and the possibility that the (cosmographic part of the) H_0 tension might actually hint to a core component coexisting with a central cusp in galaxies. In the Appendix we collect some formulae for profiles that could serve as λPL models.

2. Adding a Core to a Cusp Is an MST

Lensing analyses (Suyu et al. 2017; Birrer et al. 2019; Bonvin et al. 2019; Chen et al. 2019; Wong et al. 2019) take as input a brightness map defined on the image plane, spanned by coordinates $\boldsymbol{\theta}$, and constrain the deflection angle $\boldsymbol{\alpha}(\boldsymbol{\theta})$ given by

$$\boldsymbol{\alpha}(\boldsymbol{\theta}) = \frac{1}{\pi}\int d^2\theta' \frac{(\boldsymbol{\theta}-\boldsymbol{\theta}')}{|\boldsymbol{\theta}-\boldsymbol{\theta}'|^2}\kappa(\boldsymbol{\theta}') \tag{1}$$

via solving the lens equation

$$\boldsymbol{\beta} = \boldsymbol{\theta} - \boldsymbol{\alpha}(\boldsymbol{\theta}), \tag{2}$$

where $\boldsymbol{\beta}$ parameterizes positions on the source plane. The deflection angle is obtained by integration over the convergence,

$$\kappa(\boldsymbol{\theta}) = \frac{\Sigma(\boldsymbol{\theta})}{\Sigma_c}, \tag{3}$$

$$\Sigma_c = \frac{D_s}{4\pi G D_l D_{ls}}. \tag{4}$$

Here $\Sigma(\boldsymbol{\theta})$ is the projected surface mass density of the lens and D_s, D_l, D_{ls} are the angular diameter distances from the source to the observer, from the lens to the observer, and from the source to the lens.

Given multiple images of a quasar contained in the host galaxy, one constructs the time delay Δt_{ij} between quasar images $\boldsymbol{\theta}_i$ and $\boldsymbol{\theta}_j$,

$$\Delta t_{ij} = \mathcal{D}\Delta\tau_{ij}, \tag{5}$$

$$\Delta\tau_{ij} = \frac{\boldsymbol{\alpha}^2(\boldsymbol{\theta}_i) - \boldsymbol{\alpha}^2(\boldsymbol{\theta}_j)}{2} + \psi(\boldsymbol{\theta}_j) - \psi(\boldsymbol{\theta}_i), \tag{6}$$

$$\mathcal{D} = (1+z_l)\frac{D_s D_l}{D_{ls}}, \tag{7}$$

where

$$\psi(\boldsymbol{\theta}) = \frac{1}{\pi}\int d^2\theta' \kappa(\boldsymbol{\theta}')\ln|\boldsymbol{\theta}-\boldsymbol{\theta}'|. \tag{8}$$

If one has a model of $\kappa(\boldsymbol{\theta})$, then it can be used to calculate $\Delta\tau_{ij}$ in Equation (6). Given a measurement of Δt_{ij}, one can extract $\mathcal{D} = \Delta t_{ij}/\Delta\tau_{ij}$ and thus $H_0 \propto 1/\mathcal{D} \propto \Delta\tau_{ij}/\Delta t_{ij}$.

The MSD comes from the fact that if the lensing reconstruction problem (Equation (2)) is solved by a model for $\kappa(\boldsymbol{\theta})$, along with a model for the source position $\boldsymbol{\beta}$, then the reconstruction problem is also solved equally well by the alternative MST model[3]

$$\kappa_\lambda(\boldsymbol{\theta}) = \lambda\kappa(\boldsymbol{\theta}) + 1 - \lambda, \tag{9}$$

$$\boldsymbol{\beta}_\lambda = \lambda\boldsymbol{\beta}, \tag{10}$$

leaving $\boldsymbol{\theta}$ unchanged. While the lensing image-plane geometry is invariant under the MST, the time delay is not invariant and it is easy to verify that $\Delta\tau_{ij,\lambda} = \lambda\Delta\tau_{ij}$. This means that if we measure H_0 from some model κ, then the MST model κ_λ would give $H_0 \to (\Delta\tau_{ij,\lambda}/\Delta\tau_{ij})H_0 = \lambda H_0$.

The actual reconstruction problem of H0LiCOW deals with an extended source model, given by a map of the brightness $I_s(\boldsymbol{\beta})$ on multiple source-plane pixels. Under an MST, the distortion matrix $A_{ij}(\boldsymbol{\theta}) = \partial\beta_i/\partial\theta_j$ is rescaled to $A_{\lambda,ij}(\boldsymbol{\theta}) = \lambda A_{ij}(\boldsymbol{\theta})$, which means that the magnification $\mu = 1/\det A$ becomes $\mu_\lambda = \mu/\lambda^2$. Importantly, the relative magnification between images is unchanged. For H0LiCOW systems the precise intrinsic luminosity of the source is unknown, so absolute magnification cannot be measured. Thus extended source information does not mitigate the MSD.

The "mass sheet" in MSD refers to the $1-\lambda$ term in Equation (9), which is a constant convergence term and thus it acts as a $\boldsymbol{\theta}$-independent mass sheet. H0LiCOW took careful measures to account for the MSD due to external convergence $\kappa_{\rm ext}$ (see dedicated discussions in Suyu et al. 2017; Birrer et al. 2019; Bonvin et al. 2019; Chen et al. 2019; Wong et al. 2019). This was done by using numerical simulations to estimate the

[3] We note that the MST represents a subset of a more general set of transformations that leave the lens equation invariant (Schneider & Sluse 2014).

Table 1
Lens Systems from Millon et al. (2019)

	H_0	$\lambda = 67/H_0$	γ	θ_E ($''$)	θ_s ($''$)	Lens Redshift z_l	References
RXJ1131	$76.1^{+3.6}_{-4.3}$	$0.88^{+0.06}_{-0.04}$	1.98	1.6	19	0.295	Chen et al. (2016)
PG1115	$83.0^{+7.8}_{-7.0}$	$0.81^{+0.07}_{-0.07}$	2.18	1.1	17	0.311	Chen et al. (2019)
HE0435	$71.7^{+5.1}_{-4.6}$	$0.93^{+0.07}_{-0.06}$	1.87	1.2	10	0.4546	Chen et al. (2019)
DESJ0408	$74.6^{+2.5}_{-2.9}$	$0.9^{+0.03}_{-0.03}$	2	1.9	13	0.6	Shajib et al. (2019)
WFI2033	$72.6^{+3.3}_{-3.5}$	$0.92^{+0.05}_{-0.04}$	1.95	0.9	11	0.6575	Rusu et al. (2019)
J1206	$67.0^{+5.7}_{-4.8}$	$1^{+0.08}_{-0.08}$	1.95	1.2	4.7	0.745	Birrer et al. (2019)

Note. Values for H_0 (in km s^{-1} Mpc^{-1}) are from the PL fit (Figure 6 in Millon et al. 2019). Approximate values for the PL index γ, the Einstein radius θ_E, and the NFW scale θ_s were read from PL and composite NFW+stellar fits reported by papers in the last column.

cumulative contributions of mass along the line of sight in the field of the lens systems. However, a cored density profile (3D density $\rho \sim$ const) extending over a finite radius R_c, and dropping quickly afterward, can also give κ that is constant inside[4] $\theta \lesssim \theta_c = R_c/D_l$. Thus, if the images in the lensing data only extend over angles $\theta < \theta_c$, then the addition of a cored density component, with κ_c that is constant inside θ_c, is (i) an approximate MST, if it is done alongside a rescaling of the previous κ model, and (ii) is not equivalent to an external convergence term.[5]

To make things more concrete we define the λPL family of profiles:

$$\kappa_\lambda(\boldsymbol{\theta}) = \lambda\kappa_{\rm PL}(\boldsymbol{\theta}) + (1-\lambda)\kappa_c(\boldsymbol{\theta}). \tag{11}$$

Here, we take $\kappa_{\rm PL}$ to represent the elliptic PL profile as used by H0LiCOW to successfully model the lensing data in their systems.[6] The $\kappa_c(\boldsymbol{\theta})$ term is chosen to satisfy $\kappa_c(\boldsymbol{\theta}) \approx 1$ for $\theta < \theta_c$ and to fall faster than $\kappa_{\rm PL}$ at $\theta > \theta_c$. We do not need to assume that $\kappa_c(\boldsymbol{\theta})$ is isotropic, but in what follows for simplicity we will.

As a first example, consider the 3D cored density profile $\rho_c(r) = \frac{2}{\pi}\Sigma_c R_c^3 (R_c^2 + r^2)^{-2}$, where Σ_c is the critical density of Equation (4). The convergence for this profile is $\kappa_c(\boldsymbol{\theta}) = \left(1 + \frac{\theta^2}{\theta_c^2}\right)^{-\frac{3}{2}} = 1 - \frac{3\theta^2}{2\theta_c^2} + \mathcal{O}\left(\frac{\theta^4}{\theta_c^4}\right)$ and it induces the deflection angle $\boldsymbol{\alpha}_c(\boldsymbol{\theta}) = \hat{\theta}\frac{2\theta_c^2}{\theta}\left(1 - \left(1 + \frac{\theta^2}{\theta_c^2}\right)^{-\frac{1}{2}}\right) = \boldsymbol{\theta}\left(1 - \frac{3\theta^2}{4\theta_c^2} + \mathcal{O}\left(\frac{\theta^4}{\theta_c^4}\right)\right)$. Obviously, using this κ_c in Equation (11) gives an approximate MSD inside of $\theta < \theta_c$. We can estimate the corrections to the MSD by comparing the Einstein angle θ_E for $\kappa_{\rm PL}$ and the Einstein angle $\theta_{E\lambda}$ for κ_λ in Equation (11). For simplicity, in this exercise we take $\kappa_{\rm PL}$ to be isotropic and given by $\kappa_{\rm PL}(\boldsymbol{\theta}) = \frac{3-\gamma}{2}\frac{\theta_E^{\gamma-1}}{\theta^{\gamma-1}}$, for which the deflection angle is $\boldsymbol{\alpha}_{\rm PL}(\boldsymbol{\theta}) = \frac{\theta_E^{\gamma-1}}{\theta^{\gamma-1}}\boldsymbol{\theta}$. In the limit $\theta_c \to \infty$, the MSD is exact and $\theta_E = \theta_{E\lambda}$. For finite θ_c we find $\theta_{E\lambda} = \theta_E + \delta$, with $\delta = -\frac{3}{4(\gamma-1)}\frac{1-\lambda}{\lambda}\frac{\theta_E^2}{\theta_c^2} + \mathcal{O}\left(\frac{\theta_E^4}{\theta_c^4}\right)$. From the form of δ we can infer the parametric dependence of the breaking of the MSD. The corrections to the image-plane geometry enter at order θ^2/θ_c^2, and if $\lambda \approx 1$ (that is, if we only add a small core) are further suppressed by a factor $1 - \lambda$. Note that for real systems H0LiCOW find $\gamma \approx 2$ so $1/(\gamma - 1) \approx 1$ (see Table 1).

More generally, if in Equation (11) we use a core component that can be expanded as $\kappa_c = 1 + a\theta^2/\theta_c^2 + \ldots$ at $\theta < \theta_c$, then the leading-order image-plane corrections to the MSD at $\theta < \theta_c$ scale as $(1-\lambda)\theta^2/\theta_c^2$. This scaling remains true also when the baseline term $\kappa_{\rm PL}$ (or whatever other baseline model is considered, e.g., a composite stellar cusp+NFW model) is anisotropic.

As another example, consider the 3D cored Navarro–Frenk–White (NFW) density profile,

$$\rho_{\rm cNFW}(r) = \frac{\rho_0}{(R_c + r)(R_s + r)^2}, \tag{12}$$

which contains one extra parameter R_c, defining the core, in addition to the usual NFW density ρ_0 and scale radius R_s. The convergence $\kappa_{\rm cNFW}$ can be computed analytically even though is not particularly illuminating (in the Appendix we collect some formulae for profiles that could serve as the core component in λPL models). With proper normalization such that $\kappa_{\rm cNFW}(0) = 1$ it has the correct characteristics to function as κ_c in Equation (11). We show $\kappa_{\rm cNFW}$ by the dashed black line in Figure 1. We have set $\theta_s = R_s/D_l = 11$ and $\theta_c = 0.5\,\theta_s$, indicated by arrows at the bottom of the plot.

To illustrate the MSD, in Figure 2 we calculate the lensing geometry and time delays for a toy model of a quasar sitting in an extended host galaxy. To make things simple we replace the extended host by a circle on the source plane, centered on the quasar. We first do the lensing exercise for a pure PL model with slope $n = 1.95$ and ellipticity parameter $q = 0.8$, similar to typical H0LiCOW systems. The source-plane host "galaxy" is shown by the red circle in the top panel (source plane). The "quasar" is denoted by the magenta cross. The lensed images are shown by red lines in the bottom panel (image plane). (It is difficult to see these lines because they lie underneath the green lines of the λPL model, as explained below.) We calculate the dimensionless time delays $\Delta\tau_{ij}$ at the quasar image positions and show them next to the bottom panel (magenta, labeled PL). The convergence for this PL model (along the θ_x axis) is shown by the red line in Figure 1. We have chosen the PL normalization such that $\theta_E \approx 1$.

Next, we consider a λPL model with $\lambda = 0.75$. The convergence for this λPL model is shown by the blue line in Figure 1. The source-plane host model as given by the MSD is shown by the green circle in the top panel of Figure 2. The quasar is shown by the blue cross. The images are shown by the green line and blue crosses in the bottom panel. As expected, they sit *almost* on top of the pure PL. The time

[4] Here and elsewhere $\theta = |\boldsymbol{\theta}|$.
[5] See Schneider & Sluse (2013) for a closely related discussion.
[6] The elliptic PL profile is referred to as SPEMD in Suyu et al. (2017), Bonvin et al. (2019), Birrer et al. (2019), Chen et al. (2019), and Wong et al. (2019).

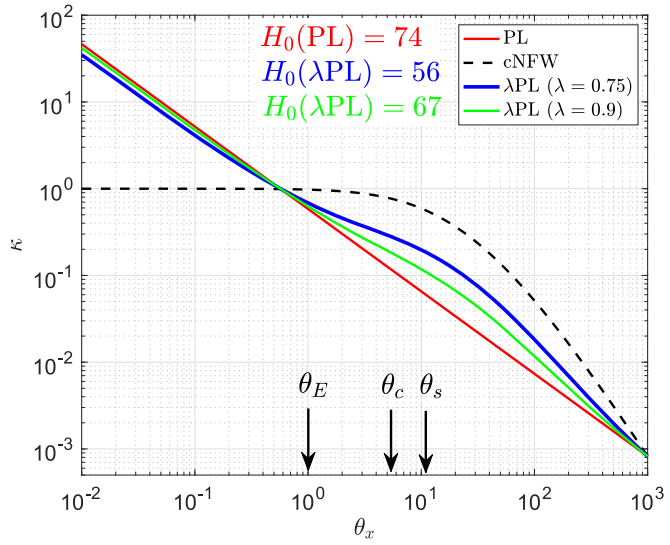

Figure 1. Convergence for a λPL model, with $\lambda = 0.75$ (blue) and $\lambda = 0.9$ (green). The $\lambda = 1$ pure PL case is shown as the red line, and the cNFW profile is shown as the black dashed line. A value of $\lambda \approx 0.9$ would bring the H0LiCOW determination of H_0 down to the CMB/LSS value. Note that for H0LiCOW lenses, both lensing and kinematics data reach outward only slightly beyond $\theta_{\rm E}$, and never constrain angles around the value of θ_c chosen in this example.

delays for the λPL model images are shown next to the bottom panel (blue, labeled λPL). As expected the λPL time delays satisfy $\Delta\tau_{ij,\lambda} \approx \lambda\Delta\tau_{ij}$.

3. If We Assume H_0 from CMB/LSS, What Do We Learn about H0LiCOW Lenses?

If one used the toy example of Figure 2 to measure H_0, and if, assuming the pure PL model, one found, for example, $H_0 = 74\ \mathrm{km\,s^{-1}\,Mpc^{-1}}$, then we expect that the λPL model with $\lambda = 0.75$ would give acceptable likelihood with $H_0 \approx 56\ \mathrm{km\,s^{-1}\,Mpc^{-1}}$. Our choice of λ in this example is, of course, an exaggeration. To solve the H_0 tension we only need $\lambda \approx 0.9$. In Table 1 we collect some key numbers for six H0LiCOW systems. Taking $H_0 \approx 67\ \mathrm{km\,s^{-1}\,Mpc^{-1}}$ to represent the CMB/LSS measurement, we show in the third column the value of λ that is required to bring the cosmographic H_0 from each system down to the CMB/LSS value.

Noting that H0LiCOW found adequate fits to the lensing reconstruction with the PL model, and given an estimate of λ for each system from Table 1, we can use Equation (11) with some models for κ_c to investigate the implied physical shape of the lens galaxies. In Figure 3 we show the results of this exercise for five systems,[7] where we use $\kappa_{\rm cNFW}$ with $\theta_s = 11''$ and $\theta_c = 5\farcs5$ to play the role of κ_c. For simplicity we ignore the ellipticity q of the PL component. Including it would shift the PL line by a constant factor of $q^{\frac{\gamma-1}{2}}$ if we project along the θ_x direction, or $q^{-\frac{\gamma-1}{2}}$ if we project along θ_y, without adjusting κ_c. Typical H0LiCOW lenses have $q \sim 0.8$ and $\gamma \sim 2$.

Considering Figure 3, it is important to note that the particular shape of the profiles at angles $\theta > \theta_{\rm E}$ is probably poorly constrained by the lensing data. Despite the fact that H0LiCOW utilizes extended host information, in practice the host image pixels do not exceed $\theta \lesssim 1.5\theta_{\rm E}$ or so. As we have seen, the impact of the edge of the core component, which breaks the MSD, enters the image plane geometry at order $(1-\lambda)\theta^2/\theta_c^2$. The λ values needed to sort out the H_0 tension imply $1-\lambda \approx 0.1$ or so for most systems; even for the most deviant system (PG1115) we have $1-\lambda \approx 0.2$. This means that $\theta_c \gtrsim 3\theta_{\rm E}$ would be enough to bring the MSD-breaking deformation down to the 1% level for most systems. Moreover, in a real analysis, some of this deformation would probably be absorbed by the fitting for the source-plane host parameters. A full-fledged analysis such as H0LiCOW, fitting λPL models to the real data, would be needed to truly quantify the level of the degeneracy. At this point, however, we emphasize that the shape of the profiles in Figure 3 at $\theta > \theta_{\rm E}$ comes from our particular choice of κ_c in this example, and is not necessitated by the data.

Finally, let us make a preliminary comparison with constraints from kinematics. Cappellari et al. (2015) presented an analysis of stellar kinematics in early-type galaxies with stellar masses in the range $\log_{10}(M_*/M_\odot) \sim 10.2$–$11.7$. These systems may be reasonable analog systems to H0LiCOW lenses. According to Cappellari et al. (2015), the total density profiles of all of the analyzed galaxies are consistent within the modeling uncertainties with simple PL all the way from $r \sim 0.1R_e$ out to $r \sim 4R_e$, where R_e is the half-light radius. This range of kinematics coverage is interesting because it overlaps with and extends the range covered by the lensing analyses, which typically probe $r \lesssim R_e$.

In Figure 4 we compare the 3D density of a λPL model with the profiles found in the galaxy kinematics analysis of Cappellari et al. (2015). The kinematics constraint, shown for the example of the system NGC 4649 (see Figure 4(d) in Cappellari et al. 2015), is given by the shaded band that envelopes a collection of 100 profiles obtained by randomly selecting model parameters from the posterior distribution of the fit. The λPL models for $\lambda = 0.9$ and $\lambda = 0.75$ are shown by solid and dashed lines, respectively. In the left panel we show the 3D equivalent of the cNFW model considered in Figures 1 and 2. In this example, the PL component in the λPL model is chosen to have[8] $\gamma = 2.25$. In the right panel we show an example where the core component of the λPL model is chosen to be a cored PL function $\rho_c \propto (R_c^2 + r^2)^{-\frac{3}{2}}$ (see the Appendix for details). In both examples we assumed $\theta_{\rm E} = \theta_e = R_e/D_l$.

The comparison of λPL models to the results from Cappellari et al. (2015) should be regarded with caution, as the family of dark matter density profiles considered in Cappellari et al. (2015) was restricted to a generalized NFW form that does not overlap with the λPL shape. With that in mind, we take Figure 4 to suggest that, currently, constraints from kinematics most likely cannot exclude λPL with $\lambda \sim 0.9$, which is the range of λ that would be implied from cosmography if one calibrated H_0 from CMB/LSS data. That said, PL-core combinations with, e.g., $\lambda = 0.75$ could perhaps be constrained by data, motivating a dedicated kinematics analysis specifically designed to test λPL profiles.

4. Discussion and Summary

Lensing data alone cannot resolve the MSD. Therefore, we think that the likelihood function in the cosmographic

[7] The sixth system—J1206 (Birrer et al. 2019)—has $\lambda = 1 \pm 0.08$, so while it would admit a $\lambda \sim 0.92$ core it is also consistent with no core component.

[8] Note that Cappellari et al. (2015) find a characteristic spectral index $\gamma > 2$ for all of their halos, while the lensing analyses typically find a softer index $\gamma < 2$.

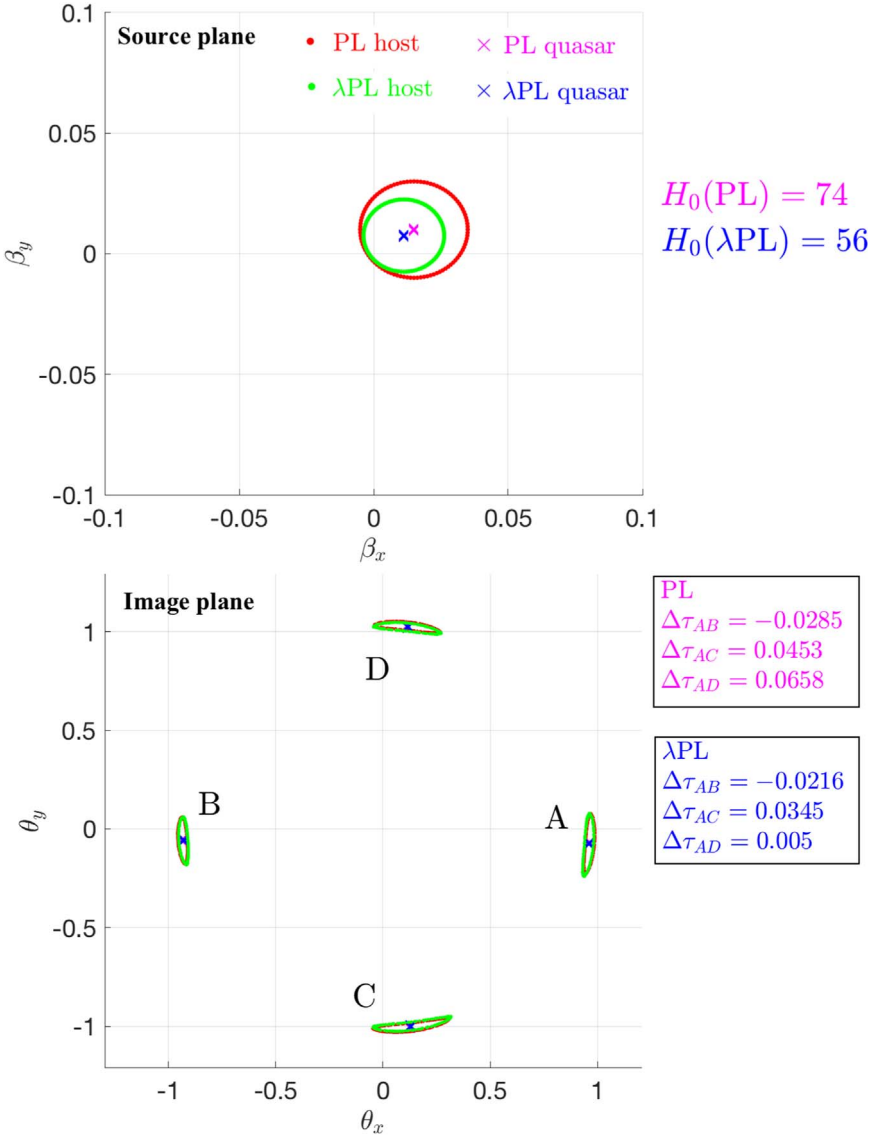

Figure 2. Example of PL-core MST for $\lambda = 0.75$. Top: source plane. Bottom: image plane. Dimensionless time delays in inset.

measurement of H_0 would have a very flat (albeit not completely flat) direction, corresponding to the effective MST λ parameter of λPL models. The H0LiCOW collaboration could thoroughly test this hypothesis on the real data. The λPL models do not require more fitting parameters than, for example, the composite stars+NFW models considered already by H0LiCOW.

Stellar velocity data do resolve the MSD and could constrain λPL models. Probably too large variations over the pure PL, in terms of the total enclosed mass, are not allowed by the stellar velocity data. However, we doubt that stellar velocity data can test an λPL model with $\lambda \approx 0.9$. Either way, if the systematic uncertainty comes to be dominated by the stellar velocity modeling, then the significance of the H_0 tension would need to be revised. In this respect, we agree with the recent discussion of Kochanek (2019).

It would be very interesting if indeed H0LiCOW has detected a core component in the lens galaxies. We are not aware of such cores in N-body or hydrodynamical simulations. Perhaps they could arise if, for example, the dark matter sector contains a component of ultralight (Schive et al. 2014) or self-interacting (Spergel & Steinhardt 2000) dark matter. On the other hand, since typical H0LiCOW lenses have $\theta_{\mathrm{E}} \ll \theta_s$ (inferred in their composite stars+NFW models), it is clear that the lensing data probe the inner part of the lens halo where baryons either dominate the dynamics or at least make a large impact on it, making the simulations challenging. From this point of view, a detection of λPL profiles with $\lambda \approx 0.9$ could be turned into a goal to explain. Before we venture to more speculations, though, it would be reassuring to see a dedicated lensing/time delay analysis that tests λPL models on the real data.

We are grateful to Michele Cappellari, Raphael Flauger, Claudio Grillo, Ranjan Laha, Sergey Sibiryakov, Yotam Soreq and, especially, Simon Birrer, Frederic Courbin, Aymeric Galan, Martin Millon, Alessandro Sonnenfeld, and Sherry Suyu for useful discussions. K.B. is incumbent of the Dewey David Stone and Harry Levine career development chair.

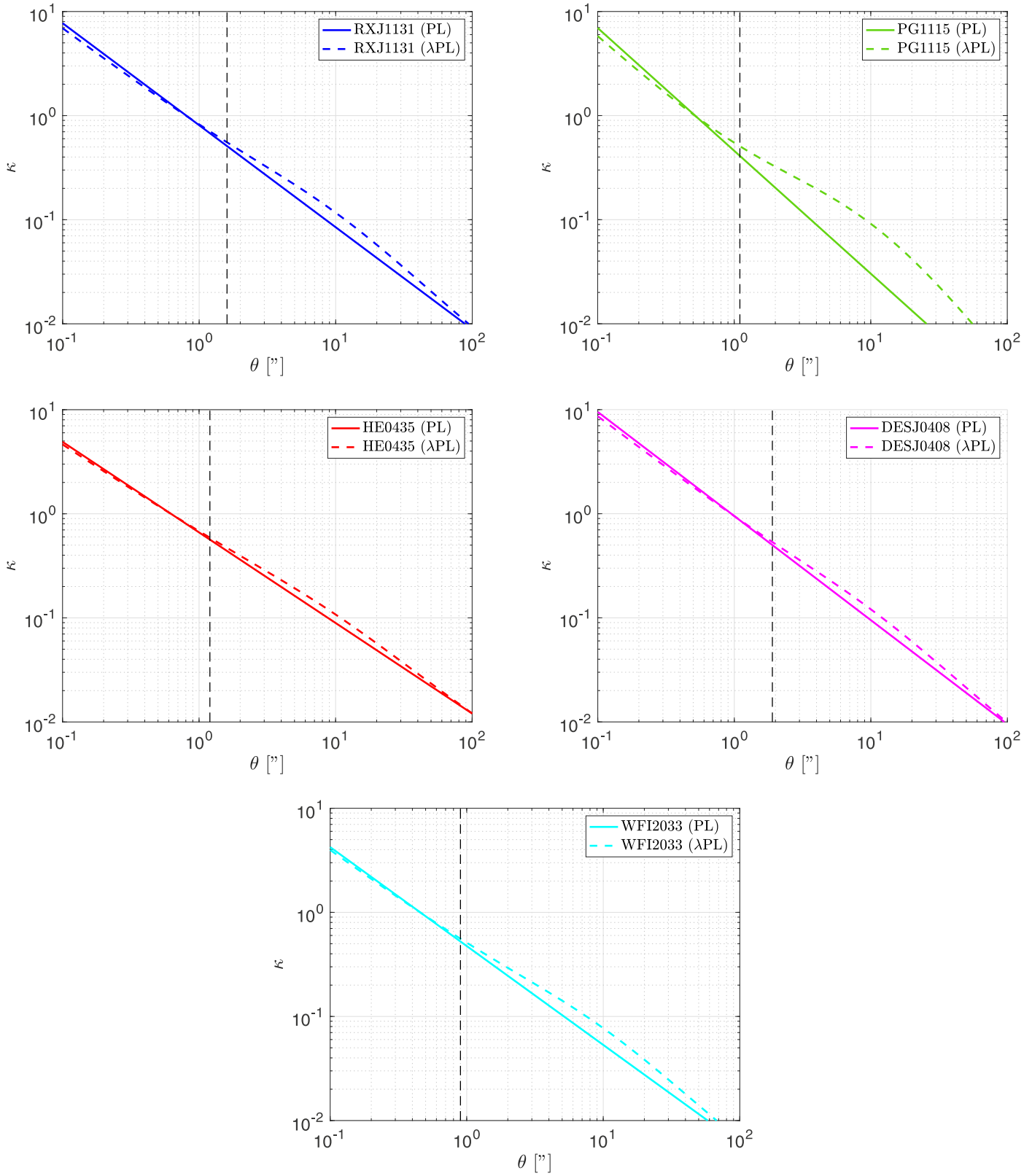

Figure 3. Inferred κ profiles (1D projection) for the lenses in Table 1. The vertical dashed line shows $\theta_{\rm E}$ for each system. The core component is cNFW.

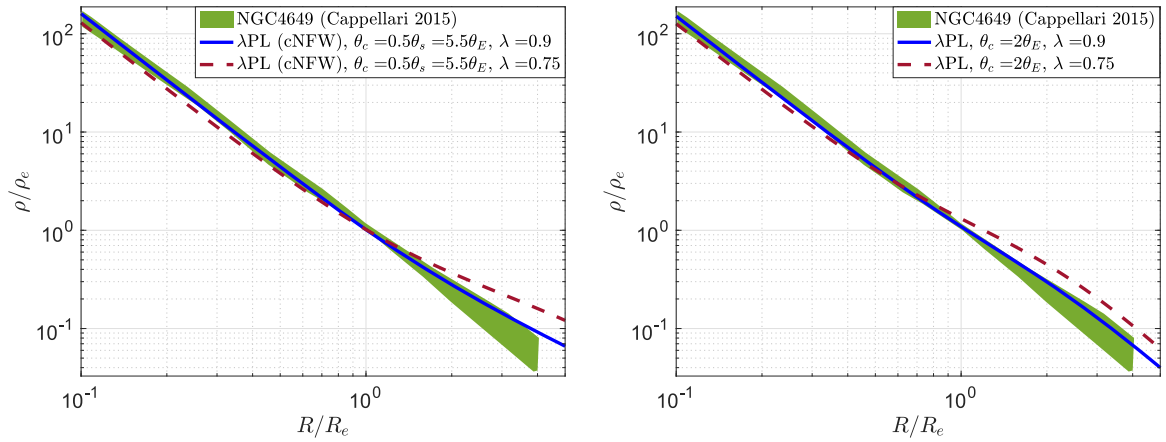

Figure 4. 3D density: comparison with constraints from kinematics. Solid (dashed) line shows the λPL profile for $\lambda = 0.9$ ($\lambda = 0.75$). Shaded band shows the posterior distribution of profiles from the kinematics fit of Cappellari et al. (2015). In this plot, for concreteness, we set $R_{\rm E} = R_e$. Left: PL+cNFW. Right: PL +cored PL.

Appendix
Some Examples of Cored Profiles

Here we first recall basic properties of the pure power-law model, relevant for lensing analyses, and then give examples of cored profiles that can be used to test our κ_c proposal. For simplicity we only consider isotropic models.

Pure power law. Consider the PL 3D isotropic density profile, designed to have projected Einstein radius $R_{\rm E}$:

$$\rho_{\rm PL}(r) = \frac{\Sigma_c}{R_{\rm E}} \frac{3-\gamma}{4\sqrt{\pi}} \frac{\Gamma\left(\frac{\gamma}{2}\right)}{\Gamma\left(\frac{\gamma-1}{2}\right)} \left(\frac{r}{R_{\rm E}}\right)^{-\gamma}. \tag{A1}$$

The convergence, deflection angle, and potential for this model are

$$\kappa_{\rm PL}(\boldsymbol{\theta}) = \frac{3-\gamma}{2}\left(\frac{\theta}{\theta_{\rm E}}\right)^{1-\gamma}, \tag{A2}$$

$$\boldsymbol{\alpha}_{\rm PL}(\boldsymbol{\theta}) = \left(\frac{\theta}{\theta_{\rm E}}\right)^{1-\gamma}\boldsymbol{\theta}, \tag{A3}$$

$$\psi_{\rm PL}(\boldsymbol{\theta}) = \frac{\theta^2}{3-\gamma}\left(\frac{\theta}{\theta_{\rm E}}\right)^{1-\gamma}. \tag{A4}$$

Cored power law. Consider

$$\rho_c(r) = \frac{\Gamma\left(\frac{\gamma}{2}\right)}{\sqrt{\pi}\,\Gamma\left(\frac{\gamma-1}{2}\right)} \frac{\Sigma_c R_c^{\gamma-1}}{(R_c^2 + r^2)^{\frac{\gamma}{2}}}. \tag{A5}$$

The convergence, deflection angle, and potential for this model are[9]

$$\kappa_c(\boldsymbol{\theta}) = \left(1 + \frac{\theta^2}{\theta_c^2}\right)^{\frac{1-\gamma}{2}}, \tag{A6}$$

$$\boldsymbol{\alpha}_c(\boldsymbol{\theta}) = \frac{2\theta_c^2}{\theta^2}\frac{\left(1+\frac{\theta^2}{\theta_c^2}\right)^{\frac{3-\gamma}{2}} - 1}{3-\gamma}\boldsymbol{\theta}, \tag{A7}$$

$$\psi_c(\boldsymbol{\theta}) = \frac{2\left(\left(1+\frac{\theta^2}{\theta_c^2}\right)^{\frac{3-\gamma}{2}} - 1\right)}{(3-\gamma)^2} - \frac{H_{\frac{\gamma-3}{2}} + 2\ln\left(\frac{\theta}{\theta_c}\right)}{3-\gamma} + \frac{\theta_c^2}{2\theta^2}\left(1+\frac{\theta^2}{\theta_c^2}\right)^{\frac{3-\gamma}{2}} \frac{\Gamma\left(\frac{\gamma-3}{2}\right)}{\Gamma\left(\frac{\gamma+1}{2}\right)} {}_2F_1\left(1, 1; \frac{\gamma+1}{2}; -\frac{\theta_c^2}{\theta^2}\right). \tag{A8}$$

Here, $H_\eta = \int_0^1 dx \frac{1-x^\eta}{1-x}$ is the harmonic number and ${}_2F_1(a, b; c; x)$ is the Gauss hypergeometric function.

Cored NFW. Consider the cored NFW profile (cNFW) with core radius

$$R_c = \zeta\, R_s, \tag{A9}$$

where ζ parameterizes the ratio between the core radius R_c and the usual NFW scale radius R_s. To use this profile as a properly normalized core component, we write the 3D density as

$$\rho_{\rm cNFW}(r) = \frac{(1-\zeta)^2}{2(\zeta - 1 - \ln\zeta)} \frac{\Sigma_c R_s^2}{(\zeta R_s + r)(R_s + r)^2}. \tag{A10}$$

For this profile we were only able to find an analytical expression for the convergence,

$$\kappa_{\rm cNFW}(\boldsymbol{\theta}) = \frac{1}{\zeta - 1 - \ln\zeta}\left(\frac{1-\zeta}{b^2-1} + \frac{2(b^2\zeta - 1)\,\mathrm{ArcCot}\left(\sqrt{\frac{b+1}{b-1}}\right)}{(b^2-1)^{3/2}} - \frac{2\zeta\,\mathrm{ArcCot}\left(\sqrt{\frac{b+\zeta}{b-\zeta}}\right)}{\sqrt{b^2-\zeta^2}}\right), \tag{A11}$$

[9] For $\gamma = 3$ we have $\boldsymbol{\alpha}_c(\boldsymbol{\theta}) = \frac{\theta_c^2}{\theta^2}\ln\left(1+\frac{\theta^2}{\theta_c^2}\right)\boldsymbol{\theta}$ and $\psi_c(\boldsymbol{\theta}) = -\frac{1}{2}\mathrm{PolyLog}\left(2, -\frac{\theta^2}{\theta_c^2}\right)$.

where we define $b = \theta/\theta_s$. Near the origin, $b \ll 1$, ζ, we have

$$\kappa_{\rm cNFW} = 1 + \frac{2(1 - 3\zeta^2 + 2\zeta^3)\ln\left(\frac{b}{2}\right) - 2\ln\zeta + \zeta^2(4\zeta - 5) + 1}{4\zeta^2(\zeta - \ln\zeta - 1)} \times b^2 + \mathcal{O}(b^4), \tag{A12}$$

as required from our definition of a $\kappa_{\rm cNFW}$ component.

Because we consider a spherical profile, the deflection angle and the potential can be obtained by the following numerical integrals:

$$\boldsymbol{\alpha}_{\rm cNFW}(\boldsymbol{\theta}) = \frac{2\hat{\theta}}{\theta}\int_0^\theta dx\, x\, \kappa_{\rm cNFW}(x), \tag{A13}$$

$$\psi_{\rm cNFW}(\boldsymbol{\theta}) = 2\int_0^\theta \frac{dy}{y}\int_0^y dx\, x\, \kappa_{\rm cNFW}(x). \tag{A14}$$

References

Abbott, T. M. C., Abdalla, F. B., Annis, J., et al. 2018, MNRAS, 480, 3879
Birrer, S., Treu, T., Rusu, C. E., et al. 2019, MNRAS, 484, 4726
Bonvin, V., Millon, M., Chan, J. H. H., et al. 2019, A&A, 629, A97
Cappellari, M., Romanowsky, A. J., Brodie, J. P., et al. 2015, ApJL, 804, L21
Chen, G. C. F., Fassnacht, C. D., Suyu, S. H., et al. 2019, MNRAS, 490, 1743
Chen, G. C. F., Suyu, S. H., Wong, K. C., et al. 2016, MNRAS, 462, 3457
D'Amico, G., Gleyzes, J., Kokron, N., et al. 2019, arXiv:1909.05271
Falco, E. E., Gorenstein, M. V., & Shapiro, I. I. 1985, ApJL, 289, L1
Freedman, W. L., Madore, B. F., Hatt, D., et al. 2019, ApJ, 882, 34
Gomer, M. R., & Williams, L. L. R. 2019, arXiv:1907.08638
Grillo, C., Rosati, P., Suyu, S. H., et al. 2018, ApJ, 860, 94
Grillo, C., Rosati, P., Suyu, S. H., et al. 2020, arXiv:2001.02232
Ivanov, M. M., Simonović, M., & Zaldarriaga, M. 2019, arXiv:1909.05277
Jee, I., Komatsu, E., & Suyu, S. 2015, JCAP, 11, 033
Jee, I., Komatsu, E., Suyu, S., & Huterer, D. 2016, JCAP, 04, 031
Kochanek, C. S. 2002, ApJ, 578, 25
Kochanek, C. S. 2006, in Saas-Fee Advanced Course 33: Gravitational Lensing: Strong, Weak and Micro, ed. G. Meylan, P. Jetzer, & P. North (Berlin: Springer), 91
Kochanek, C. S. 2019, arXiv:1911.05083
Millon, M., Galan, A., Courbin, F., et al. 2019, arXiv:1912.08027
Planck Collaboration, Akrami, Y., Arroja, F., et al. 2018, arXiv:1807.06205
Refsdal, S. 1964, MNRAS, 128, 307
Riess, A. G., Casertano, S., Yuan, W., Macri, L. M., & Scolnic, D. 2019, ApJ, 876, 85
Romanowsky, A. J., & Kochanek, C. S. 1999, ApJ, 516, 18
Rusu, C. E., Wong, K. C., Bonvin, V., et al. 2019, arXiv:1905.09338
Schive, H.-Y., Chiueh, T., & Broadhurst, T. 2014, NatPh, 10, 496
Schneider, P., & Sluse, D. 2013, A&A, 559, A37
Schneider, P., & Sluse, D. 2014, A&A, 564, A103
Shajib, A. J., Birrer, S., Treu, T., et al. 2019, arXiv:1910.06306
Shajib, A. J., Treu, T., & Agnello, A. 2018, MNRAS, 473, 210
Sonnenfeld, A. 2018, MNRAS, 474, 4648
Spergel, D. N., & Steinhardt, P. J. 2000, PhRvL, 84, 3760
Suyu, S. H., Bonvin, V., Courbin, F., et al. 2017, MNRAS, 468, 2590
Tagore, A. S., Barnes, D. J., Jackson, N., et al. 2018, MNRAS, 474, 3403
Treu, T., & Koopmans, L. V. E. 2002, MNRAS, 337, L6
Tröster, T., Sánchez, A. G., Asgari, M., et al. 2019, arXiv:1909.11006
Unruh, S., Schneider, P., & Sluse, D. 2017, A&A, 601, A77
Verde, L., Treu, T., & Riess, A. G. 2019, NatAs, 3, 891
Wong, K. C., Suyu, S. H., Chen, G. C. F., et al. 2019, arXiv:1907.04869
Xu, D., Sluse, D., Schneider, P., et al. 2016, MNRAS, 456, 739